9. P. Guo, *Molecular Dynamics Study of Single-Crystal Silicon and Aluminum the Pre-Crack Propagation*, Zhengzhou University, Zhengzhou (2007).
10. H. Rafii-Tabar, H. M. Shodja, M. Darabi, and A. Dahi, "Molecular dynamics simulation of crack propagation in fcc materials containing clusters of impurities," *Mech. Mater.*, **38**, No. 3, 243–252 (2006).
11. M. H. Musazadeh and K. Dehghani, "Molecular dynamic simulation of crack propagation in nanocrystalline Ni containing different shapes and types of second phases," *Comp. Mater. Sci.*, **50**, No. 11, 3075–3079 (2011).
12. T. Tang, S. Kim, M. F. Horstemeyer, and P. Wang, "Atomistic modeling of crack growth in magnesium single-crystal," *Eng. Fract. Mech.*, **78**, No. 1, 191–201 (2011).
13. R. Fu, Z. Y. Rui, C. F. Yan, et al., "Molecular dynamics simulation of micro-crack propagation behavior in single-crystal γ-TiAl," *J. Funct. Mater.*, **46**, No. 13, 13100–13105 (2015).
14. X. J. Wang, B. Q. Zhu, and H. M. Wang, "Effects of temperature on growth of monocrystalline aluminum crack – a molecular dynamics study," *J. Syst. Simul.*, **22**, No. 2, 534–536 (2010).
15. W. P. Wu and Z. Z. Yao, "Molecular dynamics simulation of stress distribution and microstructure evolution ahead of a growing crack in single-crystal nickel," *Theor. Appl. Fract. Mec.*, **62**, 67–75 (2012).
16. G. W. Qin and S. M. Hao, "Ti-Al system intermetallic compounds," *Rare Metal Mat. Eng.*, **24**, No. 2, 1–7 (1995).
17. S. Plimpton, "Fast parallel algorithms for short-range molecular dynamics," *J. Comput. Phys.*, **117**, No. 1, 1–19 (1995).
18. Y. F. Guo and S. W. Gao, "Atomistic simulation of crack propagationand its size-dependent behavior," *J. Northern Jiaotong Univ.*, **9**, No. 4, 5–9 (2005).
19. D. Y. Sun, M. I. Mendelev, C. A. Becker, et al., "Crystal-melt interfacial free energies in hcp metals: A molecular dynamics study of Mg," *Phys. Rev. B*, **73**, No. 2, 024116 (2006).
20. D. Faken and H. Jónsson, "Systematic analysis of local atomic structure combined with 3D computer graphics," *Comp. Mater. Sci.*, **2**, No. 2, 279–286 (1994).
21. Y. G. Zheng, J. Lu, H. W. Zhang, and Z. Chen, "Strengthening and toughening by interface-mediated slip transfer reaction in nanotwinned copper," *Scripta Mater.*, **60**, No. 7, 508–511 (2009).
22. A. Stukowski, "Visualization and analysis of atomistic simulation data with OVITO – The open visualization tool," *Model. Simul. Mater. Sc.*, **18**, No. 1, 015012 (2010).
23. S. Z. Chavoshi and X. Luo, "Molecular dynamics simulation study of deformation mechanisms in 3C–SiC during nanometric cutting at elevated temperatures," *Mater. Sci. Eng. A*, **654**, 400–417 (2016).
24. Y. F. Fu, *Molecular Dynamics studies of Plastic Deformation of Nanotwinned Copper with Embedded Cracks*, Dalian University of Technology, Dalian (2014).
25. T. Paulauskas, C. Buurma, E. Colegrove, et al., "Atomic scale study of polar Lomer–Cottrell and Hirth lock dislocation cores in CdTe," *Acta Crystallogr. A*, **70**, No. 6, 524–531 (2014).

Received 30. 08. 2016

UDC 539.4

Constitutive Behavior of 4343/4A60 Aluminum Alloy at Multi-Pass Hot Deformation

C. Tang, Y. Zhou, H. Weng, X. F. Guo, and Q. P. Xu

Guangdong University of Technology, Guangzhou, China

Hot roll bonding of 4343/4A60 aluminum alloy has been performed in the Gleeble-3500 thermal simulator. The bonding process constitutive behavior has been analyzed. The results show that the peak flow stress decreases with the increase of the deformation temperature and the decrease of strain rates. An Arrhenius-type constitutive equation is used to describe the constitutive behavior of the hot rolled 4343/4A60 aluminum alloy with the thermal deformation activation energy Q of 118.48 kJ/mol. 4A60 aluminum alloy microstructure is studied using the optical microscope to investigate the dynamic recrystallization. It is revealed that with the temperature between 573 and 623 K the dynamic recovery has an effect on modeling the microstructure evolution of 4A60 aluminum alloy. It has been also concluded that the dynamic recovery is the sole softening mechanism of 4343/4A60 composite.

Keywords: hot bonding, flow stress, constitutive behavior, microstructural evolution, dynamic recovery.

Introduction. The composite plate of 4343/4A60 aluminum alloy exhibits excellent corrosion resistance, electrical conductivity and thermal conductivity, and it serves as the transition layer between the two component metal layers in the composite [1–3]. It is widely used in a variety of heat exchangers, such as automotive radiator, car air conditioning condenser, evaporator and air cooling system of thermal power station, etc [4, 5].

With the increased deformation of hot roll bonding process the metal microstructure varies concurrently under the action of work hardening, dynamic recovery, and dynamic recrystallization [6, 7]. Plastic deformation is responsible for metal grains elongation and separation, and it causes residual stresses in metals. Thus, plastic and toughness decrease as a result of work hardening, which is not beneficial for the subsequent processing [8]. Dynamic recrystallization plays a very important role in the thermal deformation, and it causes the grain refinement that improves the mechanical properties [9]. Many studies have been conducted on the constitutive model for single metals in the deformation process. Chen et al. [10] obtained the constitutive equation of 7005 aluminum alloy. Alankar and Wells [11] investigated the constitutive equation of AA3104, AA5182, and AA6111 aluminum alloys and used the finite element software to simulate the deformation process, the results were in good agreement with the actual flow stress–strain curves. Shi [12] studied the high temperature deformation behavior of 6005A aluminum alloy and developed its constitutive model. However, the constitutive behavior of bi-metal multi-pass rolling has not been properly studied at different temperatures and strain rates. Therefore, in this paper, the flow stress–strain curves of 4343/4A60 bi-metal have been obtained by performing the hot roll bonding in the Gleeble-3500 thermal simulator. The constitutive equation of hot deformation of 4343/4A60 aluminum alloy has been investigated to provide the theoretical background for the development of hot roll bonding.

1. **Experimental Procedure**. Aluminum alloys 4343 and 4A60 are the experimental materials, which have been fully annealed. Their microstructure is presented in Fig. 1. Table 1 lists the materials' composition. The specimen dimensions are $20\times15\times5$ mm. The plane strain compression testing is carried out in the Gleeble-3500 thermal simulator (Fig. 2). The heating rate is 2°/s, the temperatures are 573, 623, 673, 723, and 773 K, respectively, the heat retention is 3 min, and the strain rates are 0.005, 0.05, 0.5, and 5 s^{-1}, respectively.

Table 1

Material Chemical Composition (wt.%)

Material	Si	Fe	Cu	Mn	Zn	Ti
4343	6.8–8.2	0.8	0.25	0.10	0.20	–
4A60	0.8	0.3	–	0.01	0.01	0.02

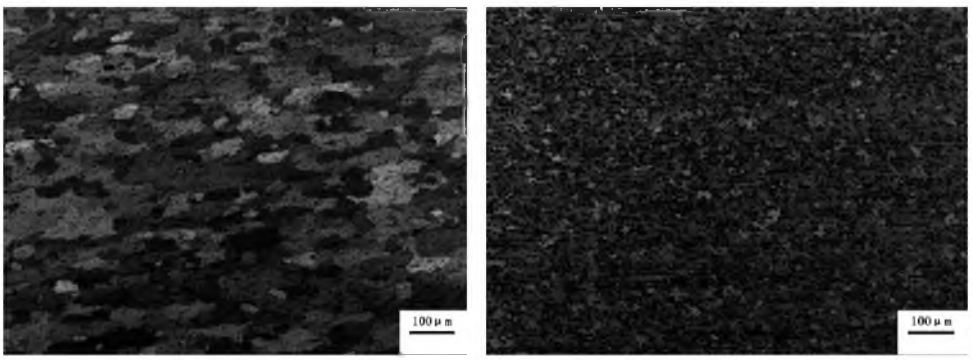

a b

Fig. 1. Original microstructure of the two aluminum alloys: 4A60 (a) and 4343 (b) aluminum alloys.

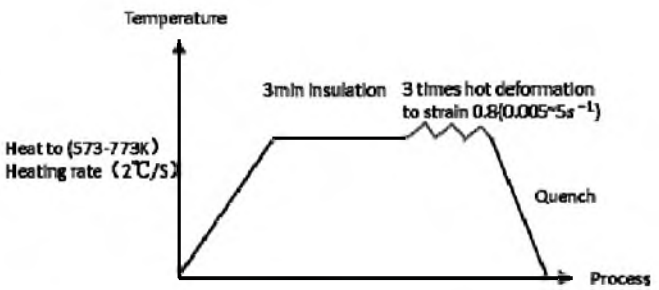

Fig. 2. Experimental process flow chart.

Too high local heating temperature can be reduced by coating the specimens with MoS_2 as well as using the pasted tantalum sheet and lubrication. The thermocouple is welded at the upper end of the specimen to provide the accurate temperature measurement. When the total strain of three passes attains the value of 0.8, the compression is stopped, and then the specimen is quenched and cooled in a vacuum to retain its high temperature deformation microstructure. The experimental process flow chart is shown in Fig. 2.

2. **Experimental Results and Analysis**.

2.1. ***True Stress–Strain Curves***. The stress–strain curves obtained from the multi-pass compression at different temperatures and strain rate are shown in Fig. 3. As it can be seen, the flow stress increases rapidly with the strain increase at the initial stage of the first pass, which is caused by the material work hardening mechanism. Moreover, the dislocation density increases with the increase of deformation, the dislocations accumulation makes the subsequent deformation more difficult, thus the stress is required to produce a greater deformation. As soon as some amount of the deformation is accumulated, the flow stress attains its peak value. The specimen rheological properties are found to be stable. At this stage, dynamic recrystallization is the main mechanism having a drastic effect on the specimen mechanical properties. The dislocations annihilation and migration are observed

with the increase of deformation. The alloy softening is caused by the dynamic recrystallization ensuring the process hardening with no general variation of the flow stress. In the following two compressions, the flow stress attained its peak value steeply and tended to be stabilized. The increase of deformation leads to the flow stress peak decrease, which might be caused by the dynamic recrystallization mechanism. The flow stress, which is required to produce the deformation, decreases, since the recrystallization softening has a greater effect as compared with the work hardening.

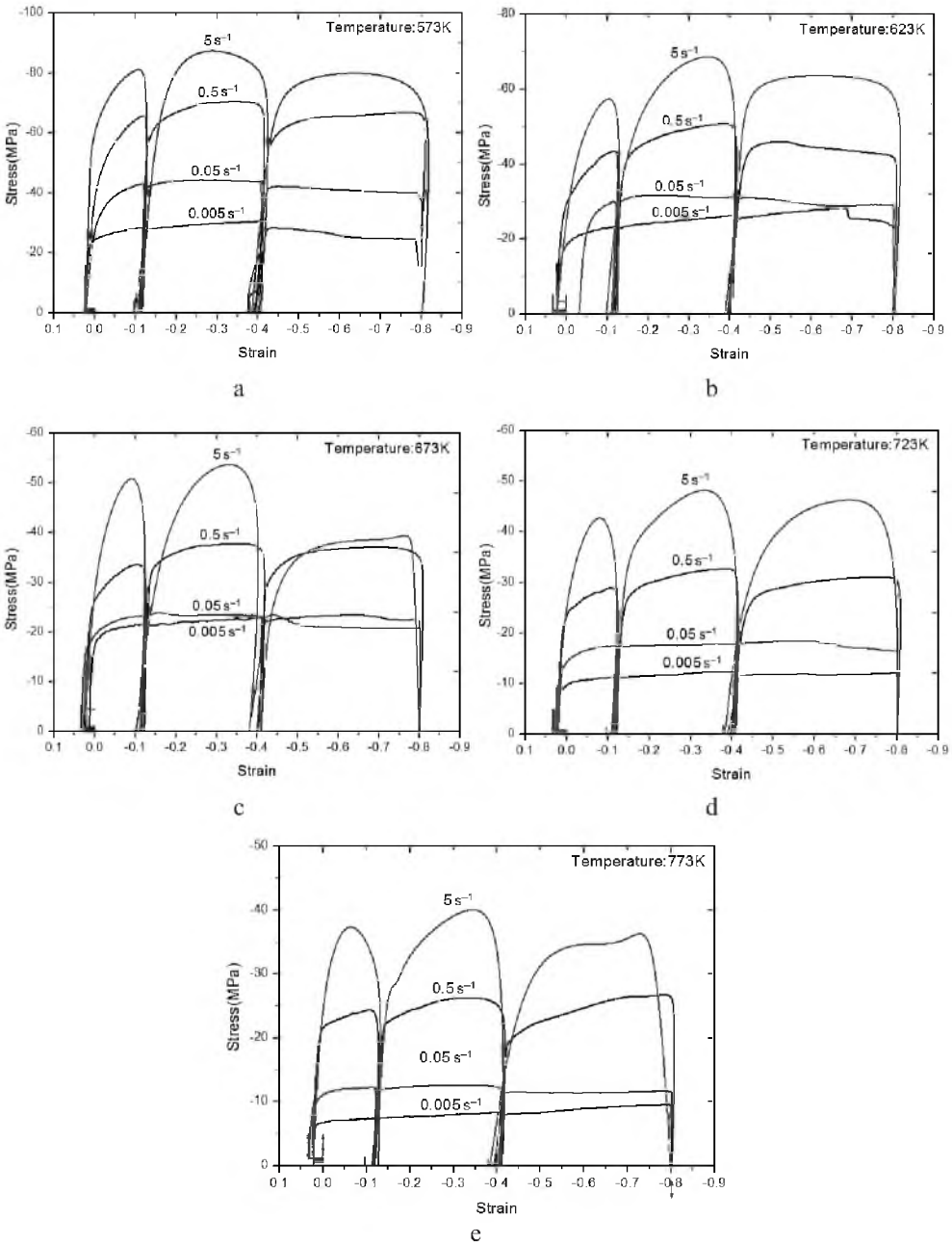

Fig. 3. True stress–strain curves obtained from the multi-pass compression under different temperature and strain rate conditions: (a) 573 K; (b) 623 K; (c) 673 K; (d) 723 K; (e) 773 K.

2.2. ***Establishment of Constitutive Equation for 4343/4A60 Aluminum Alloy Hot Rolling***.

2.2.1. *Constitutive Behavior of Single Pass Compression*. The constitutive model is used to describe the deformation behavior and to predict the flow stress in the processing. Therefore, it is of important value to the industrial production. Among several models for studying the constitutive behavior of metals, is the Arrhenius equation model, is able to accurately describe the relationship between the strain rate, deformation temperature, and flow stress [13]. Based of this, Sellars and McTegart [14] derived the hyperbolic sine (Arrhenius-type) equation for all types of the stress range, which can be expressed as

$$\dot{\varepsilon} = AF(x)\exp\left(-\frac{Q}{RT}\right). \tag{1}$$

In the equation above, function $F(x)$ equals to

$$\begin{cases} F(x) = \sigma^{n_1}, & \alpha\sigma < 0.8, \\ F(x) = \exp(\beta\sigma), & \alpha\sigma > 1.2, \\ F(x) = [\sinh(\alpha\sigma)]^n, & \text{for all } \sigma, \end{cases} \tag{2}$$

where $\dot{\varepsilon}$ is the strain rate (s^{-1}), σ is the flow stress (MPa), A, β, n, and n_1 are the constants, Q is the hot deformation activation energy (kJ/mol), R is the universal gas constant [8.31 J/(mol·K)], T is the absolute temperature (K), and α is defined as β/n_1. The effect of the temperature and the strain rate on the thermal deformation behavior can be expressed using the exponential Zener–Hollomon parameter (Z) [15]:

$$Z = \dot{\varepsilon}\exp\left(\frac{Q}{RT}\right). \tag{3}$$

According to Eqs. (1) and (3), the Zener–Holloman parameter equation can be derived as

$$Z = A[\sinh(\alpha\sigma)]^n. \tag{4}$$

To determine the values of parameters n, Q, and A, Eqs. (5), (6), and (7) are derived from Eqs. (1) and (2)

$$\dot{\varepsilon} = A_1\sigma^{n_1}\exp\left(-\frac{Q}{RT}\right), \quad \alpha\sigma < 0.8, \tag{5}$$

$$\dot{\varepsilon} = A_2\exp(\beta\sigma)\exp\left(-\frac{Q}{RT}\right), \quad \alpha\sigma > 1.2, \tag{6}$$

$$\dot{\varepsilon} = A[\sinh(\alpha\sigma)]^n\exp\left(-\frac{Q}{RT}\right), \quad \text{for all } \alpha, \tag{7}$$

where A_1 and A_2 are the temperature-independent constants; whereas the logarithm function via Eqs. (5) and (6) is derived, respectively,

$$\ln\dot{\varepsilon} = \ln A_1 + n_1\ln\sigma - \frac{Q}{RT}, \tag{8}$$

$$\ln \dot{\varepsilon} = \ln A_2 + \beta\sigma - \frac{Q}{RT}. \tag{9}$$

Using the true stress–strain results the peak stress and strain rate values can be obtained provided that the same temperature values are used in Eqs. (8) and (9). The relationships $\ln\sigma - \ln\dot{\varepsilon}$ and $\sigma - \ln\dot{\varepsilon}$, as shown in Fig. 4, are approximated by the straight line. The slopes of two straight lines in Fig. 4 are expressed as n_1 and β, respectively.

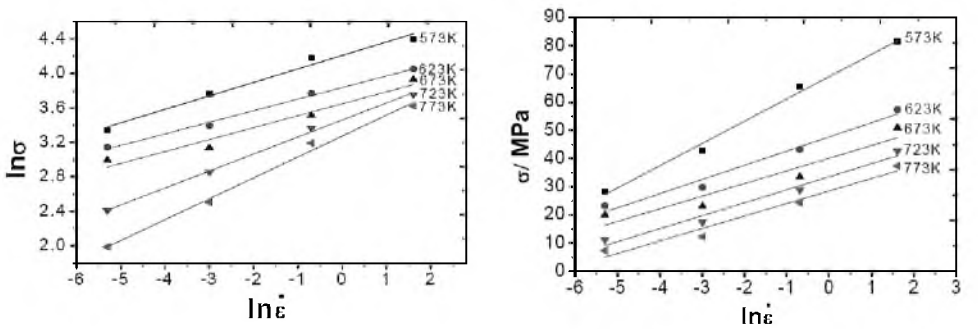

a b

Fig. 4. Dependences $\ln\sigma - \ln\dot{\varepsilon}$ (a) and $\sigma - \ln\dot{\varepsilon}$ (b).

Therefore, the average values of n_1 and β are 5.7571 and 0.1888, respectively, thereby β/n_1 is replaced with α that is 0.03278. In order to obtain the value of activation energy Q, the logarithm of Eq. (7) is taken, and the following equations are obtained

$$\ln \dot{\varepsilon} = \ln A + n \ln[\sinh(\alpha\sigma)] - \frac{Q}{RT}, \tag{10}$$

$$Q = R \left| \frac{\partial \ln \dot{\varepsilon}}{\partial \ln[\sinh(\alpha\sigma)]} \right|_T \left| \frac{\partial \ln[\sinh(\alpha\sigma)]}{\partial(1/T)} \right|_{\dot{\varepsilon}}. \tag{11}$$

The curves of $\ln\dot{\varepsilon} - \ln[\sinh(\alpha\sigma)]$ and $\ln[\sinh(\alpha\sigma)] - 1/T$ are illustrated in Fig. 5a and b, where the slopes of the straight lines are 4.34 and 3285.25. Then the activation energy Q can be of 118.48 kJ/mol in Eq. (11), which is lower in comparison with that one of aluminum alloy AA4343 Al-alloy (232.73 kJ/mol) investigated by Guo [16]. Noteworthy is that aluminum alloy AA4343 was initially used in the form of cast in the Guo experiment, while here it is in fully recrystallized state, where the metal organization is more uniform than the cast one. Therefore, the amount of activation energy required for deformation can also be decreased. To obtain the values of A and n, the value of Z can be obtained relatively to Q in Eq. (3). Equation (12) is obtained by determining the logarithm of Eq. (4):

$$\ln Z = n \ln[\sinh(\alpha\sigma)] + \ln A, \tag{12}$$

where n is the slope, $\ln A$ is the vertical intercept of the relationship line of $\ln Z - \ln[\sinh(\alpha\sigma)]$ in Fig. 5c, therefore, A and N are 1.80887 and $1.432 \cdot 10^8$, respectively. The results obtained are substituted into Eq. (7), the constitutive model of 4343/4A60 aluminum alloy composite under hot deformation conditions can be expressed as

$$\dot{\varepsilon} = 1.432 \cdot 10^8 [\sinh(0.0328\sigma)]^{1.809} \exp\left(-\frac{1.185 \cdot 10^5}{RT}\right). \tag{13}$$

The constitutive equation can be used to predict the rheological stress of 4343/4A60 aluminum alloy composite at the corresponding temperature deformation. It can be referred to the prediction of flow stress in the hot roll bonding process of 4343/4A60 aluminum alloy.

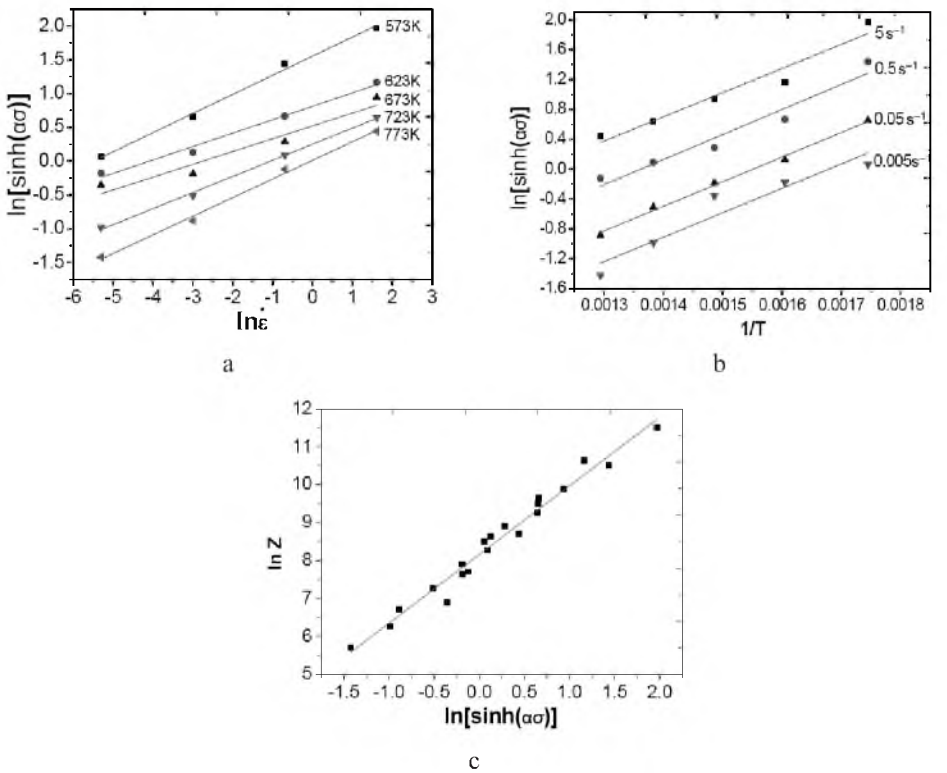

Fig. 5. Dependences $\ln\dot{\varepsilon} - \ln[\sinh(\alpha\sigma)]$ (a), $\ln[\sinh(\alpha\sigma)] - 1/T$ (b), and $\ln Z - \ln[\sinh(\alpha\sigma)]$ (c).

2.2.2. *Flow Stress of Multi-Pass Compression*. It can be seen from the stress–strain curve that in the process of multi-pass compression the flow stress peak decreases gradually with deformation, which is mainly due to the dynamic softening in the multi-pass compression. The higher the deformation temperature, the more probable is recrystallization, thus the flow stress peak became smaller. Since the degree of dynamic recrystallization directly affects the parameters of the constitutive equation, the relationships between the values of the parameters (α, $\ln A$, Q, and n) and strain (see Fig. 6) with the stress values corresponding to some strains at every 0.05 ranging from 0 to 0.8 under 0.05 strain rate and 400 are obtained from the curve. The calculation process yields

$$\begin{cases} \alpha = a_0 + a_1\varepsilon + a_2\varepsilon^2 + a_3\varepsilon^3 + a_4\varepsilon^4 + a_5\varepsilon^5 + a_6\varepsilon^6 + a_7\varepsilon^7 + a_8\varepsilon^8 + a_9\varepsilon^9, \\ Q = a_0 + a_1\varepsilon + a_2\varepsilon^2 + a_3\varepsilon^3 + a_4\varepsilon^4 + a_5\varepsilon^5 + a_6\varepsilon^6 + a_7\varepsilon^7 + a_8\varepsilon^8 + a_9\varepsilon^9, \\ n = a_0 + a_1\varepsilon + a_2\varepsilon^2 + a_3\varepsilon^3 + a_4\varepsilon^4 + a_5\varepsilon^5 + a_6\varepsilon^6 + a_7\varepsilon^7 + a_8\varepsilon^8 + a_9\varepsilon^9, \\ \ln A = a_0 + a_1\varepsilon + a_2\varepsilon^2 + a_3\varepsilon^3 + a_4\varepsilon^4 + a_5\varepsilon^5 + a_6\varepsilon^6 + a_7\varepsilon^7 + a_8\varepsilon^8 + a_9\varepsilon^9. \end{cases} \tag{14}$$

T a b l e 2

Coefficients a_0–a_9 of Eq. (14)

Parameter	a	$Q/1000$	n	$\ln A$
a_0	0.04615	149.65373	7.01159	22.5788
a_1	−0.36482	−1666.498	−110.96959	−221.02811
a_2	3.08279	22081.4	1549.194	2732.754
a_3	−1.264	−71624.3	−9815.53	−3381.73
a_4	−114.739	−342581	30545.62	−102318
a_5	681.3043	$3.12 \cdot 10^6$	$-4.11 \cdot 10^4$	$6.65 \cdot 10^5$
a_6	−1825.01	$-9.38 \cdot 10^6$	$-8.22 \cdot 10^3$	$-1.85 \cdot 10^6$
a_7	2598.216	$1.41 \cdot 10^7$	$9.22 \cdot 10^4$	$2.69 \cdot 10^6$
a_8	−1910.85	$-1.08 \cdot 10^7$	$-1.02 \cdot 10^5$	$-2.01 \cdot 10^6$
a_9	572.4184	$3.3 \cdot 10^6$	$3.71 \cdot 10^4$	$6.08 \cdot 10^5$

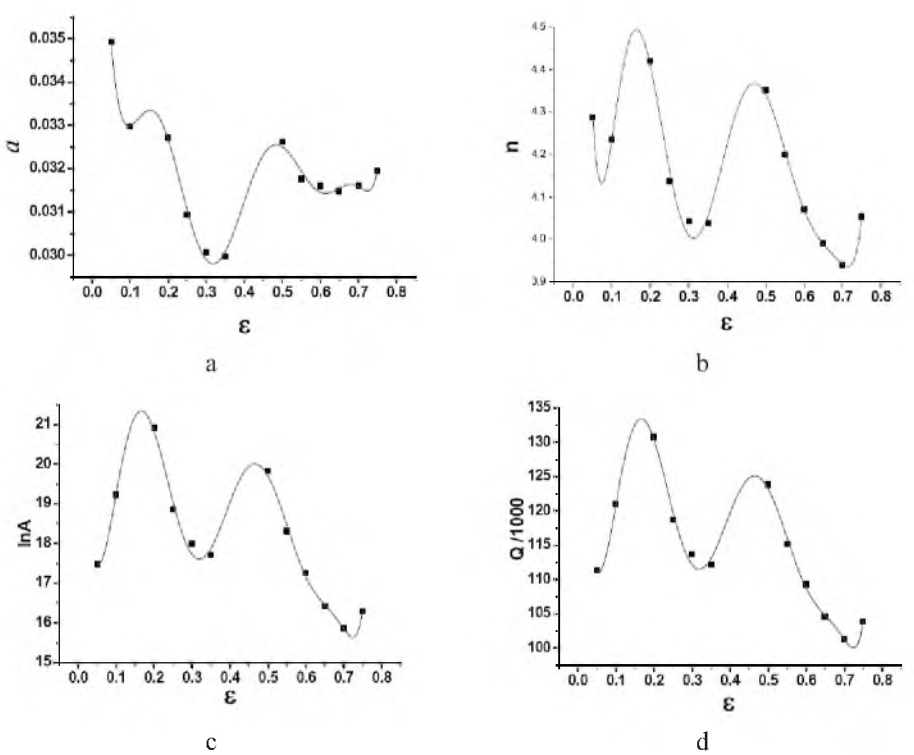

Fig. 6. Effects of parameters a (a), n (b), $\ln A$ (c), and Q (d) on ε.

The derived coefficients a_0–a_9 are tabulated in Table 2.

The results obtained from the model with the experimental stress–strain curves are shown in Fig. 7. It can be seen that the results predicted by the model are in good agreement with the experimental ones, especially when the strain ranges from 0 to 0.4, which proves that the constitutive model of bi-metal 4343/4A60 is effective. The hot deformation stress–strain behavior of 4343/4A60 can be effectively expressed by this model.

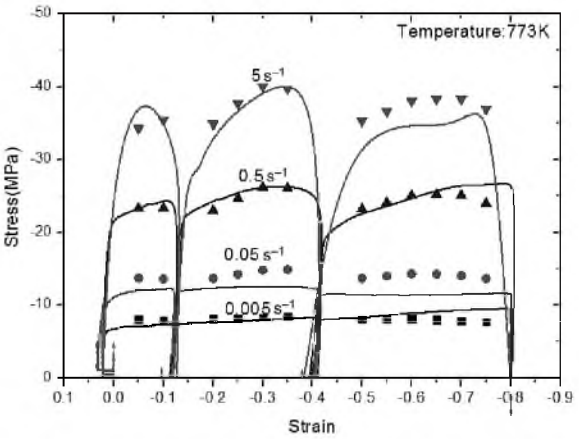

Fig. 7. Comparison of the model prediction results (solid) with the experimental results (line).

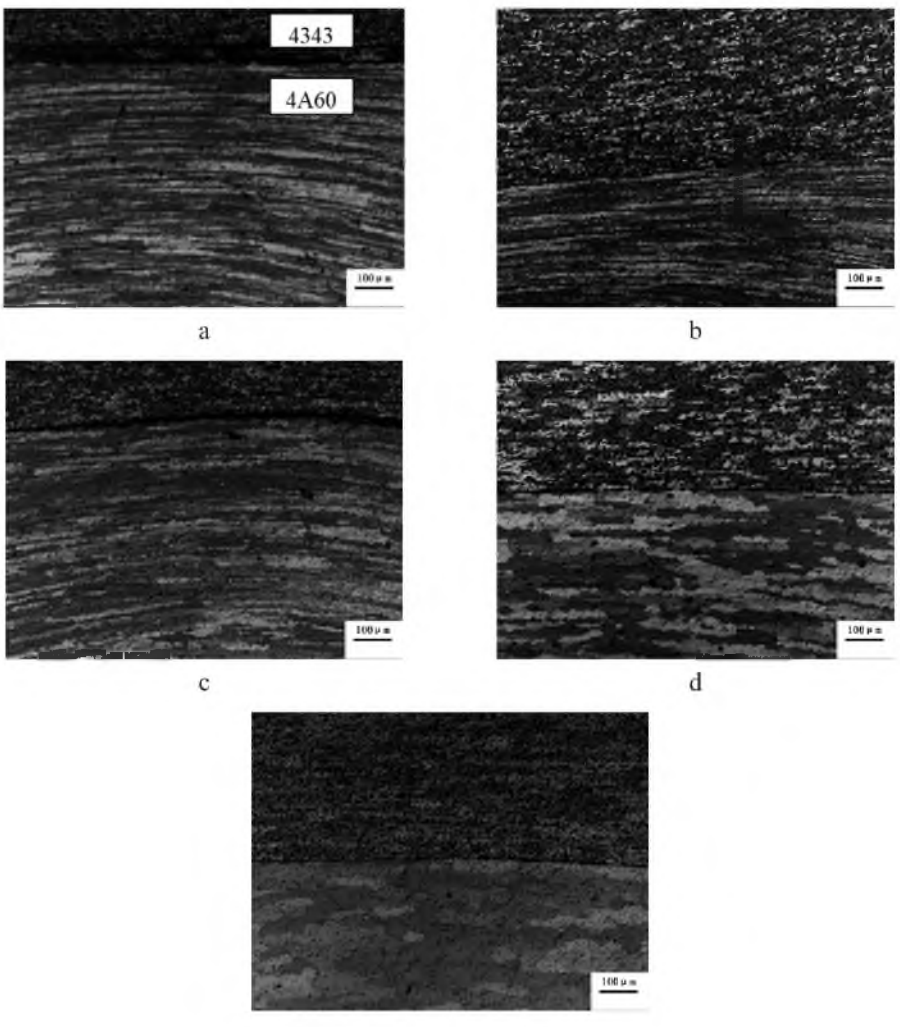

Fig. 8. Quenching microstructure after hot deformation at different temperatures: 573 (a), 623 (b), 673 (c), 723 (d) and 773 K (e).

The only drawback of this model is that for strain exceeding 0.4, there is a relatively large deviation between predicted and experimental results: explanation for a large difference between these observed at the strain rates of 0.05 and 5 requires additional research efforts.

3. **Microstructure Evolution of Thermal Deformation at Different Temperatures**. The microstructure of the quenched specimen at different deformation temperatures is shown in Fig. 8. Since silicon in 4343 aluminum alloy is 6.8~8.2%, which exceeds the solubility (1.65 wt.%) of silicon in aluminum at the eutectic temperature 850 K [17], a large number of precipitated Si particles at the grain boundaries under the microscope [18] is observed, which affects the deformation structure. After thermal deformation, the equi-axed grains of 4A60 were deformed into elongated fibrous processing structure, which was intrinsic for the observed microstructure of 4A60 Al-alloy. Within the temperature range 573–673 K, the deformation of grains increased with temperature, the recrystallization corresponds to the stage of dynamic recovery. With the temperature increase to 723 K, the grain size is significantly increased, and some isometric grains appear, whose number and size grow at temperatures above 723 K. Insofar as 4A60 aluminum alloy exhibits a significant dynamic recrystallization, which enhances its softening, the flow stress required for thermal deformation is reduced. Therefore, the dynamic recrystallization is proved to be the main mechanism for high-temperature stress reduction.

Conclusions

1. In the hot roll bonding process of 4343/4A60 in the thermal simulator, the flow stress manifests an initial rapid increase due to work hardening mechanism with the following deformation rise, the stress reaches its peak value and then remains constant, while the main deformation mechanism of this stage is dynamic recrystallization. The flow stress decreases with temperature and increases with deformation rate.

2. The constitutive model of 4343/4A60 composite in the Gleeble thermal simulator was elaborated by using the Arrhenius-type constitutive equation with the respective Zener–Hollomon parameter. Based on this, the strain-dependent constitutive model of multi-pass compression was developed. The predicted results are in a good agreement with the experimental stress–strain curves.

3. According to the microstructural investigations, dynamic recovery and dynamic recrystallization occurred in the process of deformation. Within the temperature range of 573-623K, the deformation microstructure evolution of 4343/4A60 mainly corresponds to the dynamic recovery, while at higher temperatures the dynamic recrystallization is manly observed.

Acknowledgments. This research was supported by the International Science and Technology Cooperation Project (2013DFB50170) and the National 863 Project (2013AA031301).

1. Y. Tu, Z. Tong, and J. Jiang, "Effect of microstructure on diffusional solidification of 4343/3005/4343 multi-layer aluminium brazing sheet," *Metall. Mater. Trans. A*, **44**, No. 4, 1760–1766 (2012).
2. J. Shin, K. Kim, and S. Ko, "Effects of Ti addition into core alloy on forming and brazing characteristics of 4343/3003/4343 aluminium alloy clad sheets," *Mater. T. JIM*, **54**, No. 11, 2131–2138 (2013).
3. Z. Gui, W. K. Liang, and Y. S. Zhang, "Formability of aluminium-silicon coated boron steel in hot stamping process," *Trans. Nonferr. Met. Soc.*, **24**, No. 6, 1750–1757 (2014).

4. L. Niu and Y. F. Cheng, "Electrochemical characterization of metastable pitting of 3003 aluminium alloy in ethylene glycol–water solution," *J Mater. Sci.*, **42**, No. 20, 8613–8617 (2007).
5. M. Acarer, "Electrical, corrosionand mechanical properties of aluminium-copper joints produced by explosive welding," *J Mater. Eng. Perform.*, **21**, No. 11, 2375–2379 (2012).
6. J. Luo, M. Q. Li, and D. W. Ma, "Microstructure and mechanical properties of 7A09 aluminium alloy after isothermal compression and solution treatment," *J. Mater. Process. Tech.*, **212**, No. 5, 1039–1048 (2012).
7. J. D. Robson, "Microstructural evolution in aluminium alloy 7050 during processing," *Mater. Sci. Eng. A*, **382**, 112–121 (2004).
8. C. Mondal, A. K. Singh, A. K. Mukhopadhyay, and K. Chattopadhyay, "Tensile flow and work hardening behavior of hot cross-rolled AA7010 aluminium alloy sheets," *Mater. Sci. Eng. A*, **577**, 87–100 (2013).
9. C. Castan, F. Montheillet, and A. Perlade, "Dynamic recrystallization mechanisms of an Fe–8% Al low density steel under hot rolling conditions," *Scripta Mater.*, **68**, No. 6, 360–364 (2013).
10. L. Chen, G. Q. Zhao, J. Q. Yu, and W. D. Zhang, "Constitutive analysis of homogenized 7005 aluminium alloy at evaluated temperature for extrusion process," *Mater. Design*, **66**, 129–136 (2015).
11. A. Alankar, and M. A. Wells, "Constitutive behavior of as-cast aluminium alloys AA3104, AA5182 and AA6111 at below solidus temperatures," *Mater. Sci. Eng. A*, **527**, No. 29, 7812–7820 (2010).
12. L. Shi, H. Yang, L. G. Guo, and J. Zhang, "Constitutive modeling of deformation in high temperature of a forging 6005A aluminium alloy," *Mater. Design*, **54**, 576–581 (2014).
13. J. Zhou, B. Wang, and M. Huang, "Two constitutive descriptions of boron steel 22MnB5 at high temperature," *Mater. Design*, **63**, 738–748 (2014).
14. C. M. Sellars and W. J. McG. Tegart, "La relation entre la resistance et la structure dans la deformation a chaud," *Mem. Sci. Rev. Metall.*, **63**, 731–746 (1966).
15. C. Zener and J. H. Hollomon, "Effect of strain rate upon plastic flow of steel," *J. Appl. Phys.*, **15**, 22–32 (1944).
16. J. H. Guo, S. D. Zhao, C. H. Yan, and Z. B. Wang, "Novel flow stress model of AA 4343 aluminium alloy under high temperature deformation," *Mater. Sci. Tech. Ser.*, **29**, No. 2, 197–203 (2013).
17. J. L. Murray and A. J. McAlister, "The Al-Si (Aluminum-Silicon) System," *Bull. Alloy Phase Diagrams*, **5**, 74-84 (1984).
18. T. Li, H. Zhou, S. Wang, et al., "Interface microstructure of 4343/3003/4343 aluminum alloy clad ingot prepared by liquid-solid casting," *J. Mater. Eng.*, **44**, No. 1, 19–25 (2016).

Received 30. 08. 2016